Materials Today Advances 6 (2020) 100057

Contents lists available at ScienceDirect

Materials Today Advances

journal homepage: www.journals.elsevier.com/materials-today-advances/

In situ observations of thermally induced phase transformations in iron sulfide nanoparticles

N.K. Moehring [a, b, d], M.J. Fort [a, c, d], J.R. McBride [c, d], M. Kato [e], J.E. Macdonald [c, d], P.R. Kidambi [b, d, *]

[a] Interdisciplinary Graduate Program in Materials Science, Vanderbilt University, Nashville, TN, 37235, United States
[b] Chemical and Biomolecular Engineering Department, Vanderbilt University, Nashville, TN, 37212, United States
[c] Chemistry Department, Vanderbilt University, Nashville, TN, 37235, United States
[d] Vanderbilt Institute of Nanoscale Science and Engineering, Nashville, TN, 37212, United States
[e] Mechanical Engineering Department, Vanderbilt University, Nashville, TN, 37212, United States

ARTICLE INFO

Article history:
Received 25 November 2019
Received in revised form
11 January 2020
Accepted 13 January 2020
Available online 2 March 2020

Keywords:
Iron sulfide nanoparticles
Pyrite
Pyrrhotite
In situ transmission electron microscopy (TEM)
In situ X-ray diffraction (XRD)
Phase transformation

ABSTRACT

Iron pyrite (FeS_2) exhibits dynamic thermal stability and represents an ideal model system to probe complex phase transformations in materials. At elevated temperatures, the sublimation of S atoms from the FeS_2 lattice results in a phase transformation to one of the many polymorphic forms of pyrrhotite, *i.e.*, from $Fe_{1-X}S$ (where $0 \leq X < 0.2$) to stoichiometric FeS. The complex nature of this phase transformation remains relatively unexplored at the nanoscale. Here, we use *in situ* transmission electron microscopy (TEM) and *in situ* X-ray diffraction (XRD) to observe the phase transformation of ~150 nm pyrite nanoparticles to pyrrhotite in vacuum. Although the overall shape of the nanoparticles remains cubic, the crystal structure of the nanoparticles changes from cubic pyrite to hexagonal pyrrhotite at ~400–450°C, which is ~100–150°C lower than reported values of bulk pyrite. Interestingly, our *in situ* observations do not evidence a core-shell transformation model which has been reported for the phase transformation of bulk pyrite to pyrrhotite, indicating the role of shorter length scales for diffusion in nanoparticles, as well as the role of S vacancies that facilitate faster atomic diffusion and rearrangements. In addition, the heating ramp rate was found to influence the phase transition temperature with lower temperatures of transformation seen for higher heating rates indicating the role of kinetic effects on phase transformation. We expect our detailed insights will help advance the use of FeS_2 nanoparticles in high-temperature applications including catalysis and high-temperature batteries.

1. Introduction

Phase transformation in materials are complex processes involving the dynamic interplay between thermodynamics, kinetics and material transport from the atomic scale to macroscopic length scales [1–4]. Iron sulfides in particular represent ideal model systems to probe complex multiphase transformations in materials. Iron pyrite (FeS_2), an earth abundant transition metal disulfide with an indirect bandgap of ~0.95 eV and high optical absorbance coefficient ($\alpha > 10^5$ cm^{-1}) [1–4], has attracted significant research interest for applications in photovoltaics [1,2,5], mineral processing [6], supercapacitors [3], geology [7,8], catalysis [4,8–14], and batteries [9,10,15,16]. One particular application of FeS_2 nanocrystals is in the catalysis of reactions for improving sodium-sulfur batteries operating at intermediate (100–200°C) and high temperatures (>300°C) [9,10]. The incorporation of FeS_2 nanoparticles into sodium-sulfur batteries allows for vast improvements in capacity, cycling, and better rate capability [10]. However, the chemical and physical properties which make FeS_2 nanoparticles an ideal material in this application, among others, are altered upon phase change to pyrrhotite ($Fe_{1-x}S$ where $0 \leq x < 0.2$) at high temperatures [17,18]. Hence, a comprehensive understanding of the phase stability and structural changes of FeS_2 nanoparticles is imperative to realize such high-temperature applications.

FeS_2 exhibits cubic pyrite and orthorhombic marcasite polymorphs [19,20] (Fig. S1). The pyrite crystal is similar to the NaCl structure, where there is face-centered cubic packing of S_2^{2-} dimers and Fe^{2+} cations occupying the octahedral sites [12,19]. Pyrrhotite

* Corresponding author.
E-mail address: piran.kidambi@vanderbilt.edu (P.R. Kidambi).

https://doi.org/10.1016/j.mtadv.2020.100057

($Fe_{1-x}S$ where $0 \leq x < 0.2$) [17,18] is an iron-deficient phase with monoclinic, hexagonal, and orthorhombic polymorphs [19] (Fig. S1) and its exact crystal structure is dependent on the ratio between iron and sulfur within the lattice [17,19]. The pyrrhotite phases have a structure similar to hcp packing with S^{2-} anions and Fe^{2+} cations occupying octahedral sites with varying degrees of iron vacancies. Among the many polytypes of pyrrhotite, Fe_7S_8 is the thermodynamically stable phase with both hexagonal (stable at high temperatures) and monoclinic (stable at room temperature) crystal structures [21–23]. Fe_7S_8 can be directly synthesized via chemical routes to have a perfect hexagonal macroscopic shape [19], or obtained via the decomposition of FeS_2 via heating in a non-oxidative environment [17,18].

Although research efforts have largely focused on developing synthesis methods for high purity FeS_2 nanocrystals [1,3,19,21,24], experimental studies on the phase transformation of bulk FeS_2 have typically used *ex situ* techniques such as thermogravimetric analysis (TGA) [3,25], and scanning electron microscopy (SEM) [18], with the exception of *in situ* x-ray diffraction (XRD) [17]. The emerging consensus from these studies is that upon heating cubic pyrite in a non-oxidative environment, *i.e.,* presence of inert gases (N_2) or vacuum, the S atoms in the lattice sublime and the Fe atoms rearrange to form pyrrhotite crystals with various phases and ordered iron vacancies [17–19,26]. For bulk crystals of cubic pyrite, the phase transformation to pyrrhotite typically follows a core-shell model, wherein the peripheral areas of the particles transform before the interior [15,18,26]. Specifically, TGA studies showed bulk pyrite to be stable in N_2 environment until ~600°C, with complete decomposition to pyrrhotite ~700°C [3]. Pulverized pyrite particles decomposed at lower temperatures, indicating that smaller particles have higher reactivity and significantly lower stability [25]. *In situ* XRD for particles between 75 and 125 μm in diameter showed the pyrite to pyrrhotite phase transition occurred between 550 and 600°C in inert environments [17]. Cross sectional SEM images of partially decomposed pyrite in an inert environment showed that the decomposition reaction of bulk pyrite proceeded via a core-shell model with a clear boundary between the unreacted pyrite core and reacted pyrrhotite shell [18]. Although these kinetic studies probed the phase transformation for bulk pyrite, they may not be representative of the behavior of FeS_2 at the nanoscale.

Some studies have indeed indicated differences in phase transformation for bulk FeS_2 compared with FeS_2 nanomaterials. For example, FeS_2 thin films heated under vacuum and analyzed with wide angle XRD and x-ray photoelectron spectroscopy showed phase transformation to pyrrhotite at ~400°C [27]. XRD of chemically synthesized FeS_2 nanocrystals (~14–18 nm in diameter) also indicated stability upon annealing in N_2 at temperatures below 350°C [24]. Overall, the phase transformation of cubic pyrite to pyrrhotite varies significantly from the bulk to the nanoscale and must be probed in detail to enable use of FeS_2 nanoparticles in high-temperature applications.

Here, we systematically investigate thermally induced phase transformation of cubic pyrite nanoparticles (~150 nm) in vacuum using complementary *in situ* transmission electron microscopy (TEM) and *in situ* XRD. We specifically aim to probe whether the loss of S atoms resulting in a phase change to pyrrhotite is accompanied by macroscopic changes in nanoparticle shape and if the core-shell model reported for the bulk pyrite phase transformation is seen for nanoparticles. We find the pyrite to pyrrhotite transformation occurs between 400 and 450°C for 150 nm nanoparticles, which is ~100–150°C lower than reported values of bulk pyrite. Upon heating the pyrite nanoparticles to temperatures higher than 400°C, the crystal structure of the nanoparticle is shown to approach that of hexagonal pyrrhotite. The overall shape of the particle does not change appreciably with increasing temperature and macroscopically the nanoparticle structure remains cubic. We expect our *in situ* experiments will help develop a detailed understanding of the complex pyrite phase transformations at the nanoscale and aid their use in high-temperature applications.

2. Materials and methods

2.1. Iron sulfide nanoparticle synthesis

2.1.1. Particle nucleation

To make pyrite cubes with terminated {001} surfaces, a modified version of the synthesis carried out by MacPherson and Stoldt was used [1]. Anhydrous iron chloride, $FeCl_2$, was purchased from Strem Chemicals; oleylamine (OAm, purity ~70%), hexadecylamine (purity ~90%) were purchased from Aldrich; sulfur powder (S, 99%) was purchased from Sigma-Aldrich.

Into the 100 mL 3-neck round bottom flask, 253.5 mg of $FeCl_2$ (2.0 mmol) and 384.8 mg of S (12 mmol) were added followed by 20 g of hexadecylamine. The flask was placed in a heating mantle wrapped with glass wool and foil, then placed on a Schlenk line with a chilled water condenser. The mixture was stirred at 240 rpm and the temperature was set to 250°C. Until the temperature increased above 100°C, the mixture was kept under vacuum. Once higher than 100°C, the vacuum was switched to N_2 for the remainder of the nucleation step. After 3 h at 250°C, the heat source was removed, and the mixture was allowed to return to room temperature. This allowed the hexadecylamine to solidify, preventing diffusion of the formed pyrite nuclei, and completed the pyrite particle nucleation stage.

2.1.2. Particle growth

To begin the growth stage, N_2 was left flowing over the solid hexadecylamine and nuclei mixture while the temperature was set to 70°C with the chilled water condenser constantly running. Once at 70°C, 507 mg of $FeCl_2$ (4.0 mmol), 262.9 mg of S (8.2 mmol), and 30 mL of OAm (182.4 mmol) were added under a nitrogen gas flush. Then the flask was placed under vacuum, the temperature controller was set to 200°C, and solution was stirred with a magnetic stirrer at 750 rpm. Between 70 and 100°C, the system was heated under vacuum then returned to N_2 when above 100°C. The solution was stirred at 200°C for 9 h. The heating mantle, glass wool, and foil were removed, and the flask was allowed to return to room temperature.

Twenty milliliters aliquots of the product were removed from the round bottom flask by heating the reaction vessel to 80°C under N_2 atmosphere and pipetting the solution. These samples were washed in chloroform to remove excess ligands before TEM imaging. Chloroform was added to the solution, followed by centrifugation at 8000 rpm for 5 min and the supernatant discarded. The washing procedure was repeated five times. The cleaned nanoparticles were characterized using XRD, TEM, and energy dispersive x-ray spectroscopy (EDS), then stored under nitrogen until *in situ* TEM imaging.

2.2. In situ TEM

Pyrite particle suspensions were diluted and sonicated in chloroform to reduce agglomeration. Three microliters of particle suspension was drop-cast onto a TEM grid/chip (Protochip, Aduro Thermal E-Chip) and dried in ambient environment before loading into the FEI Tecnai Osiris (200 kV) TEM (base pressure ~8.83×10^{-8} Torr). The TEM heating chips are individually calibrated by the manufacturer to have a temperature accuracy of 0.5%$\pm$1°C. Isolated,

cubic nanoparticles that were 150 nm or smaller in size were selected for imaging as they allowed for resolving lattice fringes during high resolution TEM (HR-TEM) imaging and avoided convolution of observed effects from neighboring nanoparticles, *e.g.,* Ostwald ripening.

TEM images were collected from 22°C to 600°C and the rate of temperature increase was varied from 4 to 300°C/s. At each temperature, TEM, HR-TEM, selective area electron diffraction (SAED), scanning transmission electron microscopy (STEM) and EDS were acquired. SAED patterns were collected using a 10 μm aperture. Sufficient dwell time was ensured between temperature increases to minimize effects of thermal drift confirmed via the live fast Fourier transform (FFT) during imaging. Owing to saturation of the x-ray detector at temperatures >400°C, TEM, HR-TEM, SAED, and STEM information was collected at temperature, whereas EDS spectra were collected after cooling the sample to 400°C (Fig. S2). After the EDS spectrum was collected, the temperature was again increased to the next temperature and the procedure repeated.

2.3. In situ XRD

In situ XRD measurements were performed in a Rigaku SmartLab X-Ray diffractometer using a Rigaku multipurpose high-temperature attachment and a PTC-EVO temperature controller. The x-ray diffractometer is equipped with a Cu Kα ($\lambda = 0.154$ nm) radiation source with an operating voltage of 40 kV and current of 44 mA and a D/tex Ultra 250 1D silicon strip detector. A highly concentrated solution of pyrite nanoparticles was drop-cast onto the platinum sample holder, and the solvent was allowed to evaporate. The sample temperature was increased stepwise from 22°C to 550°C with a ramp rate of 4°C/min as measured by an R-type thermocouple with an accuracy of ±1.5°C contacting the resistive Pt heater. An XRD pattern was collected every 50°C with a holding time of 3 min before and 20 min after measurement for consistency with *in situ* TEM experiments. All high-temperature sample measurements were performed under vacuum to maintain conditions similar to the *in situ* TEM chamber.

The percent phase composition and crystallite size was determined using Rietveld refinements. These were completed using whole pattern powder fitting (WPPF) in the program PDXL. Pyrrhotite is identified using JCPDS PDF# 15–1767 and pyrite identified with JCPDS PDF# 42–1340.

3. Results and discussion

3.1. Characterization of the synthesized iron sulfide nanoparticles

The synthesized nanoparticles were initially characterized using XRD to obtain nanoparticle phase and crystallite size (Fig. 1a). Fig. 1a shows the XRD pattern with peak intensities at 2Θ values corresponding to the characteristic peaks of cubic pyrite listed in literature [21]. The peaks with highest intensity are located at 2Θ values of 33.10°, 37.10°, and 56.40°. Lower intensity peaks are present at 28.50°, 40.80°, 47.40°, 59.40°, 61.90°, and 64.50°. Two relatively low intensity peaks are located at 30.10° and 43.70°, which indicate the presence of trace amounts of pyrrhotite, likely to be hexagonal FeS [28]. We assigned the trace presence of pyrrhotite to residuals from the synthesis process because FeS is a reaction intermediate [1,19].

Low magnification TEM (Fig. 1b) and high-angle annular dark-field (HAADF) images (Fig. 1d) of the pyrite nanoparticles indicate a cube-like macroscopic shape. In addition, grain boundaries within the nanoparticle in the low magnification TEM images indicate the nanoparticles are polycrystalline. HR-TEM images and respective

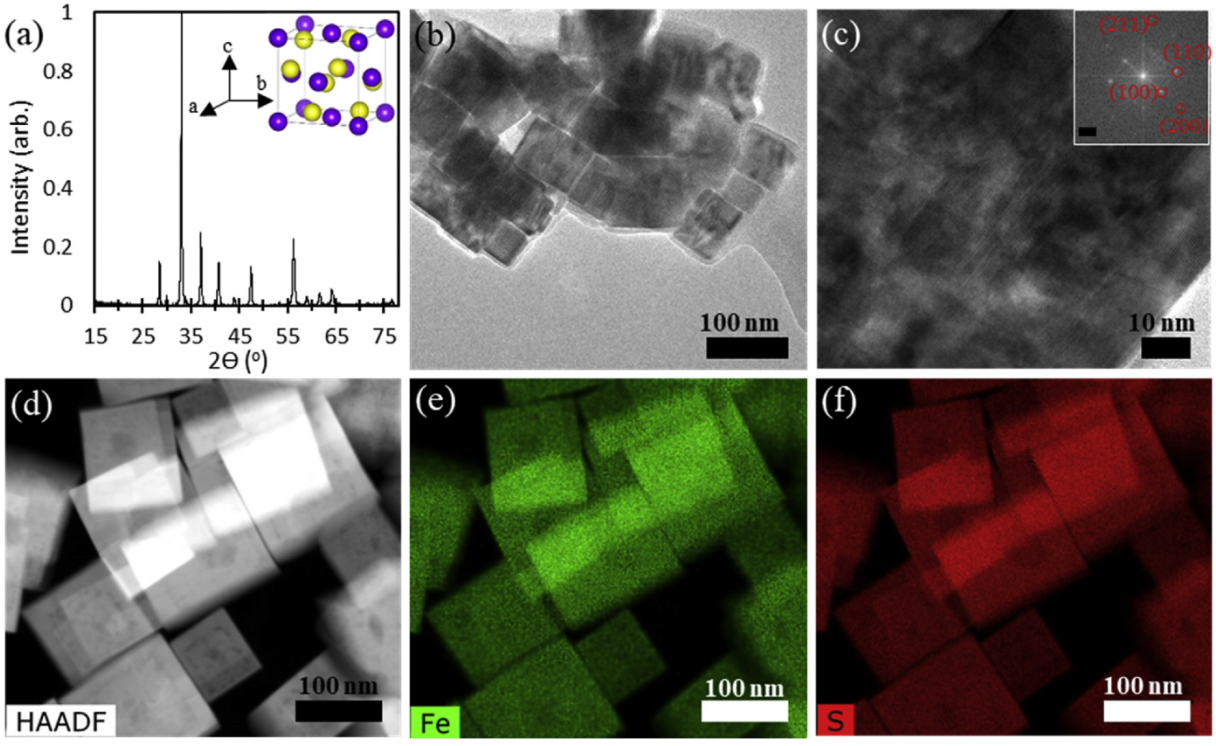

Fig. 1. Characterization of synthesized pyrite nanoparticles. (a) XRD pattern. Inset shows a model of the cubic pyrite structure, with Fe (purple) and S (yellow) atoms. (b) Bright field TEM image of pyrite nanoparticles (c) high resolution TEM image of pyrite nanoparticles. Inset shows indexed FFT of the image with scale bar of 1 nm^{-1}. (d) HAADF STEM image of pyrite nanoparticles and corresponding EDS scans of Fe (e) and S (f), respectively. TEM, transmission electron microscopy; XRD, X-ray diffraction; EDS, energy dispersive x-ray spectroscopy; STEM, scanning transmission electron microscopy; FFT, fast Fourier transform; HAADF, high-angle annular dark-field.

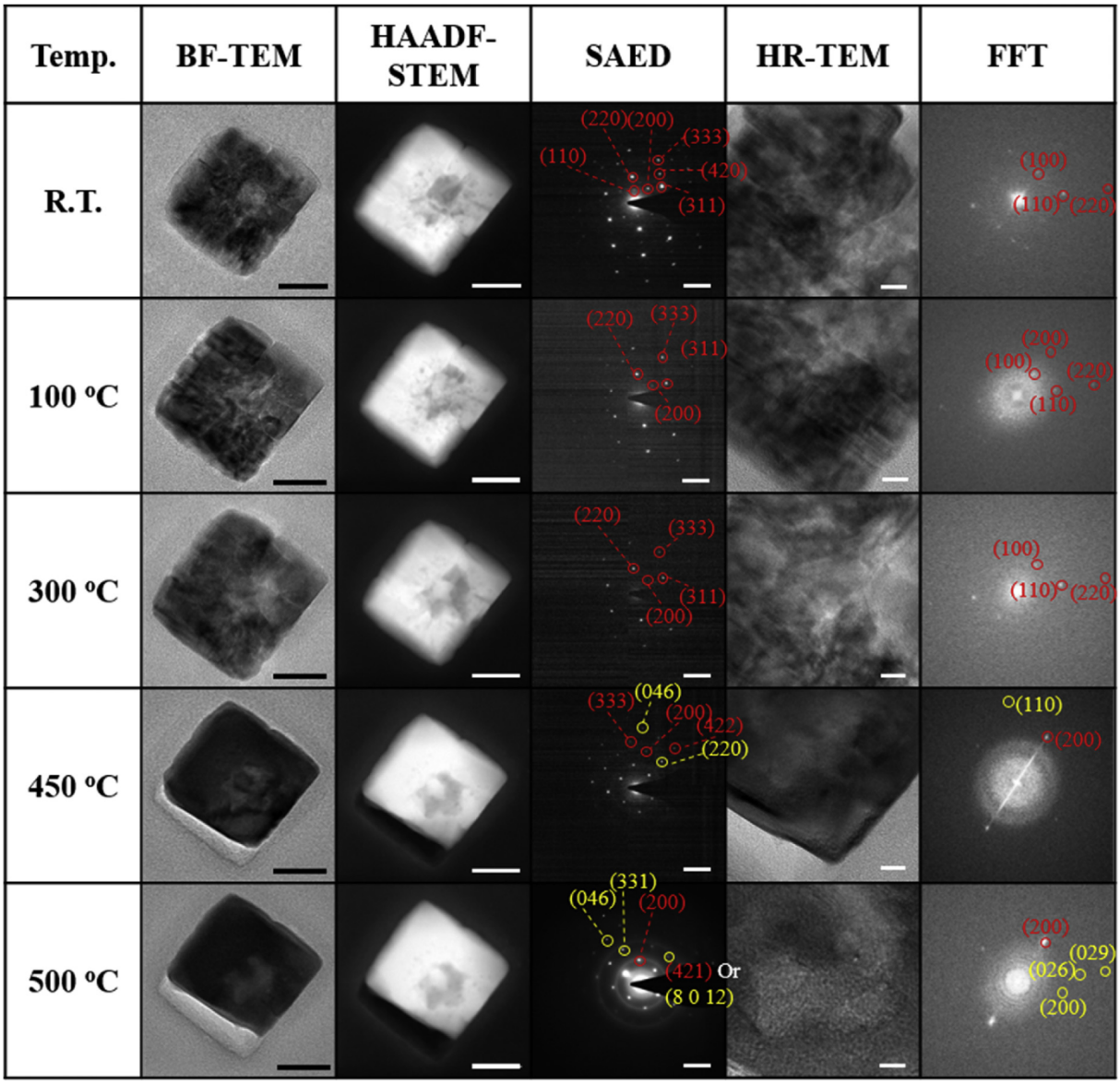

Fig. 2. Changes in nanoparticle morphology and crystal structure as heated *in situ*. Bright field TEM, HAADF STEM, SAED, HR-TEM, and the respective FFTs illustrate the changes in the nanoparticle structure. SAED was measured over the entire nanoparticle. Bright field and HAADF STEM scale bars are 50 nm. SAED scale bars are 5 nm^{-1}. HR-TEM scale bars are 10 nm. SAED and FFT spots are labeled with respective crystal planes determined by d-spacing in the literature [3,29]. Planes labeled in red represent cubic pyrite phase and planes labeled in yellow represent hexagonal pyrrhotite phase. In addition, see summary of phases and crystal planes in Fig. 3b. TEM, transmission electron microscopy; SAED, selective area electron diffraction; STEM, scanning transmission electron microscopy; FFT, fast Fourier transform; HAADF, high-angle annular dark-field.

FFTs (Fig. 1c) also shows the cubic morphology and cubic structure of the pyrite nanoparticles, respectively, with indexed diffraction spots corresponding to the (100), (110), (200), and (211) planes of cubic pyrite (Fig. 1c inset). STEM-EDS maps (Fig. 1e and f) show uniform distribution of Fe and S in the nanoparticles and allows for quantitative analysis of the atomic percent ratio of iron to sulfur (Fig. 1e and f). The atomic percent for Fe and S at room temperature is determined to be 32.65 ± 0.93% and 67.23 ± 0.90%, respectively. This ratio is in good agreement with the expected stoichiometry for pyrite (FeS_2, 33.33:66.66 of Fe:S) [21], indicating the synthesized nanoparticles are mostly cubic pyrite.

3.2. *In situ TEM*

The synthesized cubic pyrite nanoparticles were heated under vacuum (~8.83 × 10^{-8} Torr) with different rates of heating (4°C/s, 50°C/s, and 300°C/s) and bright field (BF), HAADF, HR-TEM images, SAED patterns and EDS spectra were acquired (Fig. 2 and Fig. 3). Initially at room temperature, BF and dark-field (DF) TEM images illustrate the cubic shape of the particle (Fig. 2). Phase-specific crystal planes are identified by measuring the spacing between diffraction spots in SAED pattern and HR-TEM FFTs and comparing with the reported d-spacings for each phase-specific crystal in the literature [3,22,28]. At room temperature, the measured d-spacings from the SAED pattern and HR-TEM FFTs correspond to the (100), (110), and (220) planes of cubic pyrite (Fig. S6) indicating the nanoparticle is cubic pyrite.

As the temperature is increased slowly (≤50°C/s) to 300°C, the macroscopic cubic shape of the particle remains unchanged as shown in the BF and DF TEM images and crystal planes corresponding to cubic pyrite are observed (Fig. 2). The atomic percent of Fe and S for nanoparticles heated at 4°C/s and 50°C/s to 300°C is

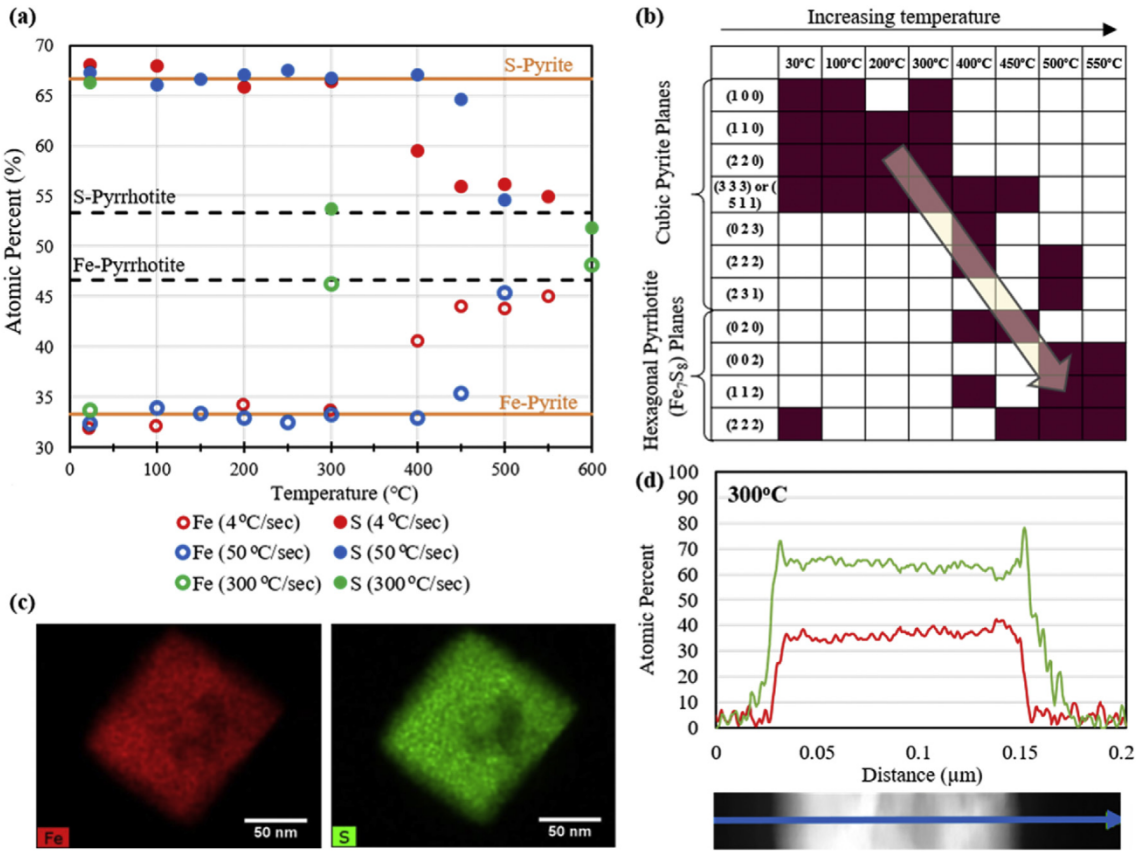

Fig. 3. Analysis of the pyrite to pyrrhotite phase transformation based on changes in elemental composition and d-spacings. (a) Normalized quantitative analysis of changes in the atomic percent of iron and sulfur composition in the nanoparticle with increasing temperature. Fe-Pyrite and S-Pyrite are reference lines representing stoichiometric at% composition of Fe and S in cubic pyrite. Similarly, Fe-Pyrrhotite and S-Pyrrhotite represent stoichiometric at% composition of Fe and S in hexagonal pyrrhotite crystal. (b) Crystal planes measured at each temperature as determined by d-spacings in SAED and HR-TEM FFTs in Fig. 2 [3,30]. A filled in box indicates the cubic or hexagonal plane measured at that temperature. Planes with d-spacings which are indistinguishable between pyrite and pyrrhotite are not included. (c) STEM-EDS micrographs at 300°C for iron (red) and sulfur (green). (d) Line scan across a nanoparticle taken at 300°C illustrating iron (red) and sulfur (green) atomic percent over a section of the nanoparticle displayed below the graph. TEM, transmission electron microscopy; EDS, energy dispersive x-ray spectroscopy; SAED, selective area electron diffraction; STEM, scanning transmission electron microscopy; FFT, fast Fourier transform.

33.44 ± 0.26% and 66.56 ± 0.26% (Fig. 3a), respectively, indicating the cubic pyrite crystal structure remains stable.

Beyond 400°C, macroscopic changes are seen in the particle (but the overall shape remains cubic) as a result of S sublimation. A 'shadow' of the original particle dimensions is visible in BF and DF TEM image, clearly illustrating the changing particle dimensions (Fig. 2). Similar observations are also seen for other particles that were only imaged at the beginning and end of the experiment, *i.e.* initially at room temperature and finally after cooling from 550°C (Fig. S4), indicating these structural features are not induced by the electron beam in combination with high temperatures. SAED and HR-TEM FFTs beyond 400°C show measured d-spacings corresponding to both cubic pyrite and hexagonal pyrrhotite, indicating a transient intermediate in the phase transformation, with coexistence of both phases (Figs. S6–S7). We note that the pyrrhotite planes in both SAED and HR-TEM FFTs are characterized based on the d-spacings reported for 3C pyrrhotite (Fig. 2) [29].

After 450°C, rings begin to appear in the SAED patterns (Fig. 2) indicating the formation of amorphous material with increasing lattice vacancies/crystal defects. At these temperatures, the atomic percent Fe and S also changes significantly, reflecting a decreasing sulfur concentration in the EDS maps of the nanoparticle (Fig. 3a, red and blue circles). As the temperature increases further, atomic percent Fe and S gradually approaches the stoichiometric atomic percent of Fe_7S_8.

At a temperature higher than 500°C, SAED and HR-TEM FFT d-spacings corresponding to both cubic pyrite and hexagonal pyrrhotite crystal planes are measured, but the frequency of occurrence of the hexagonal pyrrhotite planes is much higher than cubic pyrite (Figs. 2 and 3b). For example, the cubic pyrite (200) plane and hexagonal pyrrhotite (200), (203), (206), and (406) planes are present at 550°C. Further, we observed more hexagonal planes than cubic planes indicating the phase transformation had progressed toward hexagonal pyrrhotite. Despite the occurrence of one cubic pyrite plane, the atomic percentages of Fe and S obtained from EDS maps suggests almost complete transformation to hexagonal pyrrhotite.

When heated to 300°C rapidly (~300°C/s), the atomic percent of the nanoparticles changes abruptly to 46.27% Fe and 53.73% S, corresponding to the atomic percent of hexagonal pyrrhotite (Fig. 3a, green circles). This significant change in atomic percent is reflected in the nanoparticle morphology as well (Fig. S3). Upon further heating to 600°C, STEM images show a large chunk of the particle was rapidly lost when heated at ~300°C/s, albeit the overall macroscopic particle shape appears cubic (Fig. S3). The atomic percent extracted from the EDS spectrum indicates sulfur sublimed beyond the stoichiometric ratio of Fe_7S_8, toward that of FeS (Fig. 3a, green circles). The SAED patterns further indicate that the nanoparticle transforms from being cubic to a more disordered/nanoscale polycrystalline material (see rings and scattered diffraction in

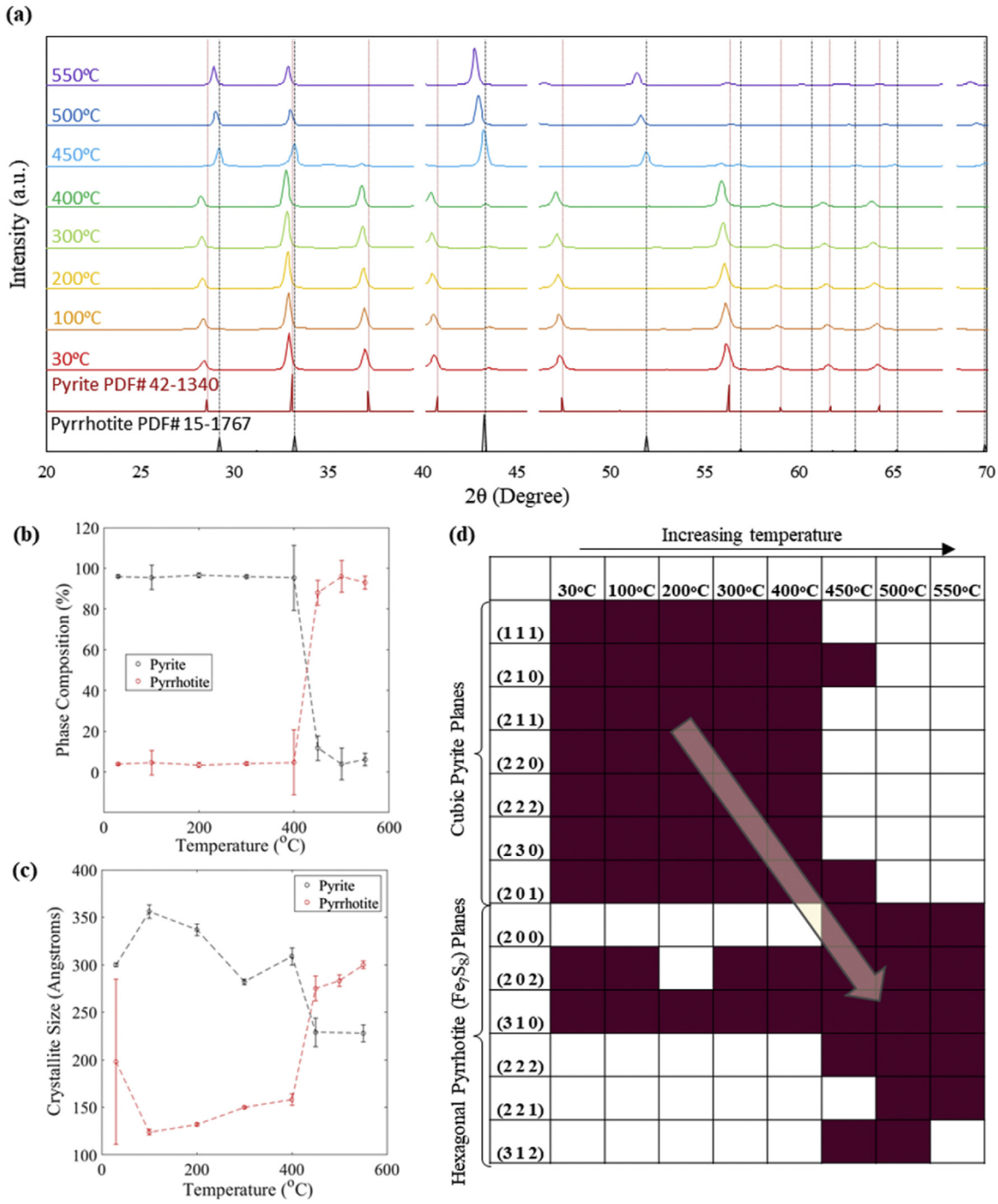

Fig. 4. Analysis of pyrite to pyrrhotite phase transformation from *in situ* XRD. (a) XRD patterns collected at room temperature to 550°C with standards patterns for pyrite and pyrrhotite plotted at the bottom. The platinum peaks at 2Θ values of 40.15°, 46.1° and 67.4° are removed from the spectra. (b) Plot of percent phase composition determined from WPPF. (c) Plot of crystallite sizes determined from WPPF. (d) Table showing presence of crystal planes measured in the XRD patterns. A filled in box indicates a peak at the 2Θ value corresponding to a certain crystal plane for cubic pyrite or hexagonal pyrrhotite [3,30]. Peaks that could not be distinguished between cubic and hexagonal planes are not included. XRD, X-ray diffraction; WPPF, whole pattern powder fitting.

Fig. S3d). The decrease in phase transformation temperature for pyrite to pyrrhotite to ~300°C upon heating rapidly ~300°C/s suggests a kinetically driven transformation. Upon rapid heating, the sulfur sublimes from the particle relatively quickly and the resulting sulfur deficient structure in unable to rearrange effectively to preserve crystalline quality as would occur when heated more slowly (Figs. 2 and 3).

Interestingly, the core/shell phase transformation model proposed for bulk particles was not observed during our study with nanoparticles. Instead, on heating the cubic pyrite nanoparticles, the entire crystal changed phase as determined by high resolution TEM and corresponding FFTs at the particle edge and at the center of the particle (Fig. S8). Between the edge and the interior of the particle, no difference is observed and the d-spacings between diffraction spots correspond to the same set of crystal planes. Typically, bulk cubic pyrite is known to transform to bulk pyrrhotite more quickly along the edges of the crystal than in the interior leading to a core/shell transformation [15,18,26].

Based on these *in situ* experiments, we show that upon heating, the cubic shape of the particle is generally maintained. The atomic percent Fe and S and the measured d-spacings in SAED and FFTs indicate a phase transformation from cubic pyrite to hexagonal pyrrhotite. The phase transformation occurs around 450°C when heated gradually (4–50°C/s) and around 300°C when heated rapidly (~300°C/s) (Fig. 3a). Overall, this transition temperature of the nanoparticles in this study is lower than that reported for bulk cubic pyrite. Literature suggests the phase transition of cubic pyrite bulk particles (grain sizes between 75 and 125 μm in diameter) to bulk pyrrhotite in an inert environment occurs ~550°C [17]. Further, pulverized cubic pyrite <1 mm particles have shown a decrease in phase transition temperatures with increased grinding time, *i.e.,* smaller particle sizes [25]. The onset of phase transition in a nitrogen environment ranged from 440°C to 362°C. Further, some cubic pyrite nanomaterials have been shown to have decomposition temperatures lower than 400°C [24,27]. Our results are in good agreement with these literature reports, suggesting a decrease in phase transition temperature with decreasing particle size. Further, the mobility of Fe and S atoms influences the phase transformation as evidenced by the rings in SAED (amorphous material) and the onset of phase change at lower temperatures with a higher heating rate. Here, we emphasize that although we evidence a phase change from cubic pyrite to hexagonal pyrrhotite upon heating, the resulting nanoparticles do not have a macroscopic hexagonal shape as is typically seen with chemically synthesized hexagonal pyrrhotite crystals [19]. Finally, we do not observe the core-shell transformation model seen for phase transformation of bulk pyrite particles to pyrrhotite in our nanoparticles [18], indicating the role of shorter length scales for diffusion in nanoparticles, as well as the role of S vacancies that facilitate faster atomic diffusion and rearrangements.

3.3. *In situ* XRD

To complement the data obtained from *in situ* TEM, the phase transformation of the iron sulfide nanoparticles was also monitored using *in situ* XRD from 30°C to 550°C. At 30°C, the XRD pattern shows peaks corresponding to 28.40°, 32.90°, 36.95°, 40.65°, 47.30°, 56.15°, 58.90°, 61.55°, and 64.20° (Fig. 4a). The peaks at 2Θ values of 40.15°, 46.10°, and 67.40° arise from the Pt sample holder and have been removed from the XRD patterns because they do not overlap with any cubic pyrite or hexagonal pyrrhotite peaks. In addition, a relatively small pyrrhotite peak is present ~43.55° indicating that the synthesized nanoparticles contain trace amounts of pyrrhotite. Using Rietveld refinement (Fig. S5), the nanoparticles are estimated with respective uncertainties to be primarily pyrite (96.09 ± 0.58% pyrite) (Fig. 4b) with large pyrite crystallite sizes (30.0 ± 0.20 nm) and smaller pyrrhotite crystallites (19.8 ± 8.7 nm) (Fig. 4c).

The XRD pattern generally remains the same until ~400°C and is consistent with *in situ* TEM for heating at 4°C/s (Figs. 2 and 3). The pyrite composition remains relatively constant in this temperature range, averaging 95.85 ± 0.53% (Fig. 4b). However, as the temperature increases, the angle at which the peaks occur in each diffraction pattern gradually decreases. For example, the peak of highest intensity for pyrite occurs at 32.90° at 30°C then decreases to 32.75° at 400°C. This downward shift in the diffraction angle is an indication of tensile strain within the crystal lattice. As the Bragg angle of diffraction decreases, the d-spacing increases, indicating strain in the lattice. We note that thermal expansion (increase in d-spacing) could also contribute toward the observed downshift in peak position. In addition, the pyrite crystallite size, determined using Rietveld refinement, fluctuates between ~30 and 35 nm, whereas the pyrrhotite crystallite size steadily increases from ~13 to ~16 nm (Fig. 4c). These crystallite sizes suggest that the particles are polycrystalline, as the crystallite sizes are smaller than the nanoparticle sizes.

At 450°C, most of the cubic pyrite peaks have disappeared, minor traces of peaks at 36.70° and 56.05°. Further, hexagonal pyrrhotite peaks at 29.20°, 33.00°, 43.25°, 51.90°, 56.85°, 63.05°, and 65.10° (Fig. 4a) appear. The percent pyrite drops to 11.7 ± 6.0% and the pyrrhotite composition increases from 4.09 ± 0.65% to 88.3 ± 6.0% (Fig. 4b). Beyond 500°C, the XRD pattern appears to be that of hexagonal pyrrhotite, with no distinguishable pyrite peaks. The pyrrhotite phase composition increases to 93.88 ± 3.1% and the crystallite size ~30.00 ± 0.40 nm is larger than the estimated pyrite crystallite size ~22.80 ± 0.90 nm. No crystallite size is reported for pyrite at 500°C because the peak of interest remains below the noise level of the XRD instrument.

The *in situ* XRD results can be directly compared with the *in situ* TEM results collected at heating rates ~4°C/s. The d-spacings obtained from SAED and HR-TEM FFTs in the *in situ* TEM study (Fig. 3b) were compared against the d-spacing obtained from the Rietveld refinement of the *in situ* XRD patterns (Fig. 4d). For pyrrhotite, the best fit XRD pattern was determined by matching patterns collected at 550°C, and $Fe_{7.04}S_8$ was found to be more appropriate fit than Fe_7S_8 [30]. Though $Fe_{7.04}S_8$ and Fe_7S_8 have a hexagonal structure, the d-spacings and corresponding planes vary owing to different degrees of Fe vacancies. Indeed, we observe excellent agreement between *in situ* XRD (Fig. 4d) and *in situ* TEM results (Fig. 3b), as both show a clear transition from mostly cubic planes to mostly hexagonal planes in the nanoparticles between 400 and 450°C.

Overall, our study indicates a kinetically driven phase transformation for cubic pyrite nanoparticles to pyrrhotite nanoparticles under vacuum. Specifically, we observe pyrrhotite particles with hexagonal atomic arrangements but macroscopic cubic forms. Upon heating at ~4°C/s, the *in situ* TEM and *in situ* XRD results are found to be in excellent agreement and phase transition temperature for cubic pyrite is ~400–450°C and the resulting product is hexagonal pyrrhotite. Upon rapid heating, the pyrrhotite product is nanoscale polycrystalline material. We emphasize that we do not observe a core-shell transformation model as seen for bulk particles.

4. Conclusion

Using *in situ* TEM and *in situ* XRD, we observe the thermally induced phase transformation of cubic pyrite nanoparticles to hexagonal pyrrhotite. Although the crystal structure of cubic pyrite nanoparticle approaches that of hexagonal pyrrhotite, the overall shape of the particle remains cubic upon heating past the transition temperature. At low ramp rates, *in situ* TEM and *in situ* XRD both indicate that the phase transition temperature for pyrite nanoparticles differs (lower by ~100–150°C) from the reported values for bulk FeS_2 [17,25]. These characteristics are important to incorporate FeS_2 nanoparticles into high-temperature applications. In addition, the diffraction rings observed in the SAED patterns and HR-TEM FFTs indicate nanoscale polycrystalline material owing to defects and/or vacancies in the crystal lattice during phase transformation, which contributes toward increased Fe and S mobility. This mobility ultimately leads to the phase transformation and can be increased by increasing the rate of heating and thereby effectively lowering the phase transition temperature. Hence, our results indicate the phase transformation of cubic pyrite to hexagonal pyrrhotite is kinetically driven. Finally, we do not observe the core-shell transformation model seen for phase transformation of bulk pyrite particles to pyrrhotite in our nanoparticles, indicating the role of shorter length scales for diffusion in nanoparticles, as well as

the role of S vacancies that facilitate faster atomic diffusion and rearrangements. We expect our detailed insights will help advance the use of FeS_2 nanoparticles in high-temperature applications including high-temperature batteries, catalysis, among others. Future studies analyzing phase transformations of cubic pyrite upon exposure to heat in atmospheric conditions could potentially use these results to decouple the effect of temperature and associated phase transformation into pyrrhotite from the transformation to other compounds such as hematite and magnetite.

Author credit statement

P.R.K. conceived the project and designed the experiments. J.R.M., N.M, and M.K, performed the *in situ* TEM experiments. M.F. and J.E.M. synthesized the nanoparticles and performed the *in situ* XRD experiments. All authors contributed to discussions and data analysis. P.R.K. and N.M. wrote the manuscript with input from all the co-authors.

Declaration of competing interest

The authors declare that they have no known competing financial interests or personal relationships that could have appeared to influence the work reported in this article.

Acknowledgements

The use of Vanderbilt Institute of Nanoscale Science and Engineering CORE facilities is acknowledged. This work was supported by American Chemical Society Petroleum Research Fund Doctoral New Investigator Grant number 59267-DNI10 and Vanderbilt University faculty start-up funds to P.R.K and J.E.M.

Appendix A. Supplementary data

Supplementary data to this article can be found online at https://doi.org/10.1016/j.mtadv.2020.100057.

References

[1] H.A. MacPherson, C.R. Stoldt, Iron pyrite nanocubes: size and shape considerations for photovoltaic application, ACS Nano 6 (2012) 8940–8949, https://doi.org/10.1021/nn3029502.
[2] S. Shukla, J.W. Ager, Q. Xiong, T. Sritharan, Scientific and technological assessment of iron pyrite for use in solar devices, Energy Technol. 6 (2018) 8–20, https://doi.org/10.1002/ente.201700638.
[3] S. Venkateshalu, P.G. Kumar, P. Kollu, S.K. Jeong, A.N. Grace, Solvothermal synthesis and electrochemical properties of phase pure pyrite FeS_2 for supercapacitor applications, Electrochim. Acta 290 (2018) 378–389, https://doi.org/10.1016/j.electacta.2018.09.027.
[4] D. Heift, Iron sulfide materials: catalysts for electrochemical hydrogen evolution, Inorga 7 (2019) 75, https://doi.org/10.3390/inorganics7060075.
[5] A. Kirkeminde, S. Ren, Thermodynamic control of iron pyrite nanocrystal synthesis with high photoactivity and stability, J. Mater. Chem. A. 1 (2013) 49–54, https://doi.org/10.1039/c2ta00498d.
[6] A. Starling, J.M. Gilligan, A.H.C. Carter, R.P. Foster, R.A. Saunders, High-temperature hydrothermal precipitation of precious metals on the surface of pyrite, Nature 340 (1989) 298–300, https://doi.org/10.1038/340298a0.
[7] Y.H. Chen, Y.H. Chen, W.D. Hsu, Y.C. Chang, H.S. Sheu, J.J. Lee, S.K. Lin, Using the high-temperature phase transition of iron sulfide minerals as an indicator of fault slip temperature, Sci. Rep. 9 (2019) 7950, https://doi.org/10.1038/s41598-019-44319-8.
[8] A. Matamoros-Veloza, O. Cespedes, B.R.G. Johnson, T.M. Stawski, U. Terranova, N.H. de Leeuw, L.G. Benning, A highly reactive precursor in the iron sulfide system, Nat. Commun. 9 (2018) 3125, https://doi.org/10.1038/s41467-018-05493-x.
[9] K.B. Hueso, M. Armand, T. Rojo, High temperature sodium batteries: status, challenges and future trends, Energy Environ. Sci. 6 (2013) 734–749, https://doi.org/10.1039/c3ee24086j.
[10] A. Douglas, R. Carter, L. Oakes, K. Share, A.P. Cohn, C.L. Pint, Ultrafine iron pyrite (FeS_2) nanocrystals improve sodium-sulfur and lithium-sulfur conversion reactions for efficient batteries, ACS Nano 9 (2015) 11156–11165, https://doi.org/10.1021/acsnano.5b04700.
[11] G. Nikiforidis, M.C.M. van de Sanden, M.N. Tsampas, High and intermediate temperature sodium-sulfur batteries for energy storage: development, challenges and perspectives, RSC Adv. 9 (2019) 5649–5673, https://doi.org/10.1039/c8ra08658c.
[12] M.R. Gao, Y.R. Zheng, J. Jiang, S.H. Yu, Pyrite-type nanomaterials for advanced electrocatalysis, Acc. Chem. Res. 50 (2017) 2194–2204, https://doi.org/10.1021/acs.accounts.7b00187.
[13] R. Miao, B. Dutta, S. Sahoo, J. He, W. Zhong, S.A. Cetegen, T. Jiang, S.P. Alpay, S.L. Suib, Mesoporous iron sulfide for highly efficient electrocatalytic hydrogen evolution the phase purity of the, J. Am. Chem. Soc. 139 (2017) 13604–13607, https://doi.org/10.1021/jacs.7b07044.
[14] M. Villalba, J. Peron, M. Giraud, C. Tard, pH-dependence on HER electrocatalytic activity of iron sulfide pyrite nanoparticles, Electrochem. Commun. 91 (2018) 10–14, https://doi.org/10.1016/j.elecom.2018.04.019.
[15] P.J. Masset, Thermal stability of FeS_2 cathode material in “thermal” batteries: effect of dissolved oxides in molten salt electrolytes, Z. Naturforsch. 63 (2008) 596–601, https://doi.org/10.1515/zna-2008-0911.
[16] Y. Tan, K.W. Wong, Z. Zhang, K.M. Ng, In situ synthesis of iron sulfide embedded porous carbon hollow spheres for sodium ion batteries, Nanoscale 9 (2017) 19408–19414, https://doi.org/10.1039/c7nr06886g.
[17] S.K. Bhargava, A. Garg, N.D. Subasinghe, In situ high-temperature phase transformation studies on pyrite, Fuel 88 (2009) 988–993, https://doi.org/10.1016/j.fuel.2008.12.005.
[18] G. Hu, K. Dam-Johansen, S. Wedel, J.P. Hansen, Decomposition and oxidation of pyrite, Prog. Energy Combust. Sci. 32 (2006) 295–314, https://doi.org/10.1016/j.pecs.2005.11.004.
[19] J.M. Rhodes, C.A. Jones, L.B. Thal, J.E. Macdonald, Phase-controlled colloidal syntheses of iron sulfide nanocrystals via sulfur precursor reactivity and direct pyrite precipitation, Chem. Mater. 29 (2017) 8521–8530, https://doi.org/10.1021/acs.chemmater.7b03550.
[20] V.K. Gudelli, V. Kanchana, S. Appalakondaiah, G. Vaitheeswaran, M.C. Valsakumar, Phase stability and thermoelectric properties of the mineral FeS_2: an ab initio study, J. Phys. Chem. C 117 (2013) 21120–21131, https://doi.org/10.1021/jp406928v.
[21] G. Willeke, O. Blenk, Ch Kloc, E. Bucher, Preparation and electrical transport properties of pyrite (FeS_2) single crystals, J. Alloys Compd. 178 (1992) 181–191, https://doi.org/10.1016/0925-8388(92)90260-G.
[22] M. Tokonami, K. Nishiguchi, N. Morimoto, Crystal structure of a monoclinic pyrrhotite (Fe_7S_8), Am. Mineral. 57 (1972) 1066–1080.
[23] J. Deng, S. Wen, X. Chen, Y. Xian, D. Wu, Dynamic simulation of the thermal decomposition of pyrite under vacuum, Metall. Mater. Trans. 45A (2014) 2445–2452, https://doi.org/10.1007/s11661-014-2206-4.
[24] S.C. Hsiao, C.M. Hsu, S.Y. Chen, Y.H. Perng, Y.L. Chueh, L.J. Chen, L.H. Chou, Facile synthesis and characterization of high temperature phase FeS_2 pyrite nanocrystals, Mater. Lett. 75 (2012) 152–154, https://doi.org/10.1016/j.matlet.2012.02.033.
[25] H. Hu, Q. Chen, Z. Yin, P. Zhang, Thermal behaviors of mechanically activated pyrites by thermogravimetry (TG), Thermochim. Acta 398 (2003) 233–240, https://doi.org/10.1016/S0040-6031(02)00390-8.
[26] P. Toulmin, P.B. Barton, A thermodynamic study of pyrite and pyrrhotite, Geochimica et Cosmochimica 28 (1963) 641–671, https://doi.org/10.1016/0016-7037(64)90083-3.
[27] X. Zhang, T. Scott, T. Socha, D. Nielsen, M. Manno, M. Johnson, Y. Yan, Y. Losovyj, P. Dowben, E.S. Aydil, C. Leighton, Phase stability and stoichiometry in thin film iron pyrite: impact on electronic transport properties, ACS Appl. Mater. Interfaces 7 (2015) 14130–14139, https://doi.org/10.1021/acsami.5b03422.
[28] O. Kruse, Phase transitions and kinetics in natural FeS measured by X-ray diffraction and Mssbauer spectroscopy at elevated temperatures, Am. Mineral. 77 (1992) 391–398.
[29] A. Nakano, M. Tokonami, N. Morimoto, Refinement of 3C pyrrhotite, Fe7S8, Acta Crystallogr. B35 (1979) 722–724, https://doi.org/10.1107/S0567740879004532.
[30] A.V. Powell, P. Vaqueiro, K.S. Knight, L.C. Chapon, R.D. Sánchez, Structure and magnetism in synthetic pyrrhotite Fe_7S_8: a powder neutron-diffraction study, Phys. Rev. B 70 (2004) 1–12, https://doi.org/10.1103/PhysRevB.70.014415.